

# Well-behaved dynamics in a dissipative nonideal periodically kicked rotator

R. Chacón

*Departamento de Electrónica e Ingeniería Electromecánica, Escuela de Ingenierías Industriales,  
Universidad de Extremadura, Apartado Postal 382, E-06071 Badajoz, Spain*

A. Martínez García-Hoz

*Departamento de Física Aplicada, Escuela Universitaria Politécnica, Universidad de Castilla-La Mancha,  
E-13400 Almadén (Ciudad Real), Spain*

(Received 29 July 2003; published 31 December 2003)

Well-behaved dynamical properties are found in a dissipative kicked rotator subjected to a periodic string of asymmetric pulses of *finite* amplitude and width. The stability boundaries of the equilibrium are determined to arbitrary approximation for trigonometric pulses by means of circular harmonic balance, and to first approximation for general elliptic pulses by means of an elliptic harmonic balance method. The bifurcation behavior at the stability boundaries is determined numerically. We show how the extension of the instability region of the equilibrium in pulse parameter space reaches a maximum as the pulse width is varied. We also characterize the dependence of the mean duration of the transients to the equilibrium on the pulse width. The evolution of the basins of attraction of chaotic attractors when solely the pulse width is varied is characterized numerically. Finally, we show that the order-chaos route when solely the width of the pulses is altered appears to be especially rich, including different types of crises. The mechanism underlying these reshaping-induced crises is discussed with the aid of a two-dimensional map.

DOI: 10.1103/PhysRevE.68.066217

PACS number(s): 05.45.Ac, 05.45.Pq

## I. INTRODUCTION

Nonlinear nonautonomous dynamical systems, subjected to a periodic string of pulses, describe a vast variety of physical, chemical, biological, and neuronal phenomena [1–3], to cite only a few. The choice of a specific mathematical function to model a given real-world pulse determines, to a great extent, the range of phenomena that it could suitably characterize. In this regard, the periodic  $\delta$  function provides a simple but rather ideal model of a periodic string of asymmetric pulses. It has generally been used in the context of systems subjected to periodic impacts. The periodically kicked rotator, for instance, has been (and still is) an extensively investigated paradigmatic example [4]:

$$\frac{d^2x}{dt^2} + \eta \frac{dx}{dt} + F(\sin x) \sum_{n=0}^{\infty} \delta(t - nT) = 0, \quad (1)$$

where  $x$  is the angular coordinate,  $\eta$  is a normalized damping coefficient,  $F$  is the normalized amplitude, and time (and hence period) have been normalized in units of  $\omega_0^{-1}$  ( $\omega_0$  being the small-angle resonant frequency of the underlying integrable pendulum). As is well known, the main advantage of employing the  $\delta$  function is that Eq. (1) (and other similar equations) can be reduced to a two-dimensional map [4–10], so that analytical and numerical results are readily obtained in these cases [11]. It is clear, however, that a deeper understanding of diverse dynamical phenomena leads one to introduce mathematical models for *nonideal* pulses into dynamical equations, i.e., pulses with *finite* width and amplitude. In this respect, a comparison of the behavior of a damped pendulum driven by a periodic string of pulses modeled first by the Jacobian elliptic function (JEF)  $\text{dn}$ , and then by a periodic  $\delta$  function is discussed in Ref. [12]. A numerical study

of a damped Duffing oscillator subjected to an external force represented by the JEF  $\text{cn}$  is given in Ref. [13].

In this present work, we discuss well-behaved properties of the dissipative nonideal periodically kicked rotator (NIPKR) which was introduced in Ref. [14]:

$$\frac{d^2x}{dt^2} + \eta \frac{dx}{dt} + F(\sin x)p(t; T, \alpha_i) = 0, \quad (2)$$

where  $p(t; T, \alpha_i)$  is a generic asymmetric pulse [i.e.,  $p(t = (2n-1)T/2; T, \alpha_i) = 0$ ,  $n = 1, 2, \dots$ ;  $p(t; T, \alpha_i) > 0$ , otherwise] of unit amplitude, period  $T$ , and wave form controlled by the parameters  $\alpha_i$ . All variables and parameters are dimensionless. Equation (2) always possesses the stationary solution ( $x=0, dx/dt=0$ ), which, however, need not be stable against small perturbations. While Eq. (2) permits us to study the structural stability of the system solely under changes of the shape of the pulse function (i.e., with fixed amplitude and period), this degree of freedom is absent in the model of Eq. (1). In this paper, we shall deal only with pulse functions which could represent realistic impacts, i.e., pulse functions having a *single* maximum. A physical condition concerning the impulse transmitted by this type of pulse, for the dynamics of the kicked rotator (2) to be independent of the particular wave form of the pulse, was discussed in Ref. [14]: it is that any two asymmetric single-maximum pulse functions  $p(t; T, \alpha_i), p'(t; T, \alpha'_i)$  yield the same impulse in the sense

$$\int_0^T p(t; T, \alpha_i) dt = \int_0^T p'(t; T, \alpha'_i) dt. \quad (3)$$

It was demonstrated that the smaller the (time-dimensional) period of the pulse relative to the small-angle period of the

underlying integrable pendulum (i.e.,  $T < 1$ ), the better the invariance condition (3) works. As numerical experiments show that the invariance condition (3) is approximately correct for pulse functions modeling real-world impacts even for periods that are not small (cf. Ref. [14]), we shall hereafter use the choice of pulse function [15]

$$p(t; T, m) \equiv \frac{\text{dn}(2Kt/T; m) - \sqrt{1-m}}{1 - \sqrt{1-m}} \quad (4)$$

to obtain generic findings that are (approximately) valid for that type of pulse. In Eq. (4),  $\text{dn}$  is the JEF of parameter  $m$ ,  $K \equiv K(m)$  is the complete elliptic integral of the first kind [16], and  $T$  is the period of the pulses. Our choice of the pulse function (4) is motivated by three remarkable properties. First, the shape of the pulse (and hence the effective width) is changed by solely varying a *single* parameter, the elliptic parameter  $m$ , between 0 and 1. Second, when  $m = 0$ , then  $p(t; T, m = 0) = \cos^2(\pi t/T)$ , i.e., we recover the simplest harmonic representation for an asymmetric pulse. In this trigonometric limiting case, Eq. (2) represents a parametrically forced gravitational pendulum with a vertically oscillating support:  $d^2x/dt^2 + \eta dx/dt + (F/2)[1 + \cos(2\pi t/T)]\sin x = 0$  [17]. This limiting case has been extensively studied by several authors [18–26]. And third, by increasing  $m$  the effective width of the pulse becomes ever lower, and for  $m \lesssim 1$  we recover a periodic sharply kicking excitation very close to the periodic  $\delta$  function, but with *finite* width and amplitude as in real-world impacts.

The organization of the rest of the paper is as follows. In Sec. II we determine the stability boundaries for the stationary solution ( $x = 0, dx/dt = 0$ ) in the parameter space  $(\eta, F, T, m)$ . The theoretical approach is based on the assumption that the stability boundaries of Eq. (2) can be obtained by analytically solving its linearized equation. We separately consider the cases of general elliptic ( $0 \leq m < 1$ ) and trigonometric ( $m = 0$ ) pulses. For the former case, we additionally assume that the truncation of certain generalized Fourier series at lowest order provides an approximate but useful solution of the aforementioned linearized equation. We demonstrate that the extension of the instability region of the stationary solution ( $x = 0, dx/dt = 0$ ) in the  $T$ - $F$  parameter plane reaches a maximum as the pulse width is varied. We found that, for any pulse width, the duration of the transients to such a stationary solution fits a sigmoidal (Boltzmann) function. Also, we compare the stability boundaries in the  $T$ - $F$  parameter plane with the respective (for each tongue) chaotic boundaries. Numerical simulations are then employed to investigate the manner in which the basins of attraction of chaotic attractors evolve as the pulse width is changed. Section III gives a characterization of the generic chaos-order route found as the pulse width is decreased (i.e., when  $m$  is varied from 0 to 1), the remaining parameters being held constant. We also discuss the mechanism underlying the reshaping-induced crises by using a simple two-dimensional map. In addition, we briefly discuss the bifurcation behavior at the stability boundaries when the period is the only parameter changed. Finally, in Sec. IV we give a few concluding remarks.

## II. STABILITY BOUNDARIES FOR THE EQUILIBRIUM

In this section we assume that the normalized period  $T$  is not too large (typically,  $T \leq 10$ ) for the invariance condition (3) to be approximately correct. One can then obtain theoretical estimates of the stability boundaries for the solution ( $x = 0, dx/dt = 0$ ), which would be valid for any symmetric-pulse function  $p(t; T, \alpha_i)$ . For the sake of clarity, we shall treat separately the cases of trigonometric pulses ( $m = 0$ ) and (general) elliptic pulses ( $0 \leq m < 1$ ).

### A. Case of trigonometric pulses

For trigonometric pulses ( $m = 0$ ) we rewrite the NIPKR (2),(4) as

$$\Omega^2 \frac{d^2x}{d\tau^2} + q \frac{dx}{d\tau} + \varepsilon [1 + \cos(2\tau)] \sin x = 0, \quad (5)$$

using the transformations

$$\tau = \frac{1}{2} \omega t, \quad \Omega = \frac{\omega}{2}, \quad q = \eta \Omega, \quad \varepsilon = \frac{F}{2}, \quad (6)$$

where  $\omega = 2\pi/T$ . The linearized equation for a perturbation  $\xi$  around the stationary solution ( $x = 0, dx/dt = 0$ ) reads

$$\Omega^2 \frac{d^2\xi}{d\tau^2} + q \frac{d\xi}{d\tau} + \varepsilon [1 + \cos(2\tau)] \xi = 0. \quad (7)$$

We assume that the stability boundary may be determined from the existence of a periodic solution for  $\xi$ . According to Floquet's theorem [27], a Floquet multiplier must vanish at the stability boundaries. Thus we may assume the existence of

$$\xi = A_0 + \sum_{n=1}^{\infty} (A_n \cos n\tau + B_n \sin n\tau). \quad (8)$$

Inserting relation (8) into Eq. (7), by balancing harmonics, we obtain

$$(\varepsilon - n^2 \Omega^2) A_n + nq B_n + \frac{\varepsilon}{2} (A_{n-2} + A_{n+2} + A_0 \delta_{2n}) = 0,$$

$$(\varepsilon - n^2 \Omega^2) B_n - nq A_n + \frac{\varepsilon}{2} (B_{n-2} + B_{n+2}) = 0, \quad (9)$$

where  $\delta_{nm}$  is the Kronecker delta, and where we have used the identities  $A_{-n} = A_n$  and  $B_{-n} = -B_n$ . For the lowest-order approximation we truncate Eq. (9) at  $n = 1$ . We then obtain the following two equations:

$$\left( \frac{3}{2} \varepsilon - \Omega^2 \right) A_1 + q B_1 = 0,$$

$$-q A_1 + \left( \frac{\varepsilon}{2} - \Omega^2 \right) B_1 = 0. \quad (10)$$

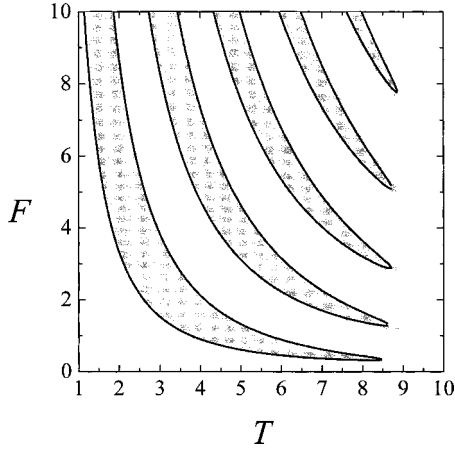


FIG. 1. Stability boundaries of the solution  $x=dx/dt=0$  in the  $T$ - $F$  parameter plane for trigonometric pulses ( $m=0$ ) and  $\eta=0.2$ . Instability regions (gray areas) were numerically calculated on a grid of  $300 \times 300$  points. Black lines denote the stability boundaries obtained theoretically at truncation  $n=10$  from Eq. (9).  $T$  and  $F$  are dimensionless parameters.

The existence of a nontrivial solution requires the determinant of the coefficients to vanish:

$$\begin{vmatrix} \frac{3\varepsilon}{2} - \Omega^2 & q \\ -q & \frac{\varepsilon}{2} - \Omega^2 \end{vmatrix} = 0, \quad (11)$$

which gives [cf. Eq. (6)]

$$F = F^{(1)}(\eta, T) \equiv \frac{4\pi^2}{3T^2} \left[ 2 \pm \sqrt{1 - \frac{3\eta^2 T^2}{\pi^2}} \right]. \quad (12)$$

Any finite higher-order approximation  $F^{(n)}(\eta, T)$  of the stability boundaries in the  $T$ - $F$  parameter plane can be found from Eq. (9). Numerical simulations indeed show that the accuracy of the theoretical estimates increases as  $n$  is increased. As an example, Fig. 1 shows the numerically calculated instability regions (gray areas) and the stability bound-

aries (black lines) obtained at the truncation  $n=10$  for  $\eta=0.2$ . To numerically obtain the instability regions we used a grid of  $300 \times 300$  points in the  $T$ - $F$  parameter plane. For each of the 90 000 points, we integrated up to 400 drive cycles and the behavior in the last few cycles was examined to plot a point on the grid when  $|x| > 10^{-6}$  or  $|dx/dt| > 10^{-6}$ . Note that the tenth-order approximation only goes slightly wrong in how accurately it reproduces the tips of the (boundary of the) tongues' tails.

### B. Case of general elliptic pulses

For general elliptic pulses ( $m \in [0, 1[$ ) the analog of Eq. (5) is

$$\Omega^2 \frac{d^2 x}{d\tau^2} + q \frac{dx}{d\tau} + 2\varepsilon \frac{\text{dn}(\tau; m) - \sqrt{1-m}}{1 - \sqrt{1-m}} \sin x = 0, \quad (13)$$

where we have used the transformations (6) with  $\omega = \omega(m) \equiv 4K(m)/T$ , while the associated linearized equation is

$$\Omega^2 \frac{d^2 \xi}{d\tau^2} + q \frac{d\xi}{d\tau} + 2\varepsilon \frac{\text{dn}(\tau; m) - \sqrt{1-m}}{1 - \sqrt{1-m}} \xi = 0. \quad (14)$$

We assume (as for trigonometric pulses) that the stability boundaries may be determined from the existence of a periodic solution for  $\xi$ . For the present general case we use an elliptic generalization of Floquet's theorem, which is based on the existence of generalized Fourier series [28] and on an elliptic harmonic balance method [29]. Thus we may assume the existence of

$$\xi = \frac{A_0}{2} + \sum_{n=1}^{\infty} [A_n \cos(n\varphi) + B_n \sin(n\varphi)], \quad (15)$$

where  $\varphi \equiv \text{am}(\tau; m)$  is the JEF of the parameter  $m$ . To obtain a preliminary estimate of the stability boundaries in the  $m$ - $F$  and  $T$ - $F$  parameter planes, we shall limit our treatment to the lowest-order approximation. Thus we truncate the series (15) at  $n=1$  and insert the resulting expression into Eq. (14), obtaining

$$\left\{ \Omega^2 [(2m-1)\text{cn}(\tau) - 2m\text{cn}^3(\tau)] - q\text{sn}(\tau)\text{dn}(\tau) + 2\varepsilon \frac{\text{dn}(\tau) - \sqrt{1-m}}{1 - \sqrt{1-m}} \text{cn}(\tau) \right\} A_1 + \left\{ \Omega^2 [-(1+m)\text{sn}(\tau) + 2m\text{sn}^3(\tau)] + q\text{cn}(\tau)\text{dn}(\tau) + 2\varepsilon \frac{\text{dn}(\tau) - \sqrt{1-m}}{1 - \sqrt{1-m}} \text{sn}(\tau) \right\} B_1 + \varepsilon \frac{\text{dn}(\tau) - \sqrt{1-m}}{1 - \sqrt{1-m}} A_0 = 0, \quad (16)$$

where we have used  $\sin \varphi \equiv \text{sn}(\tau; m)$ ,  $\cos \varphi \equiv \text{cn}(\tau; m)$  [ $\text{sn}(\tau; m)$  and  $\text{cn}(\tau; m)$  are JEFs of the parameter  $m$ ] and the notation  $pq(\tau) \equiv pq(\tau; m)$ . By using the generalized Fourier series [28] for the function  $\text{dn}(\tau)$  and for the above products of JEFs (see the Appendix), if the expansions are limited to the lowest order, instead of Eq. (16) we have

$$\left\{ \left[ \Omega^2 \left( \frac{m}{2} - 1 \right) + 2\varepsilon \frac{a_1(m) - \sqrt{1-m}}{1 - \sqrt{1-m}} \right] A_1 + q a_1(m) B_1 \right\} \cos \varphi + \left\{ -q b_1(m) A_1 + \left[ \Omega^2 \left( \frac{m}{2} - 1 \right) + 2\varepsilon \frac{b_1(m) - \sqrt{1-m}}{1 - \sqrt{1-m}} \right] B_1 \right\} \sin \varphi + \varepsilon \frac{a_0(m) - \sqrt{1-m}}{1 - \sqrt{1-m}} + (\text{higher harmonics}) = 0, \quad (17)$$

where  $a_0(m)$ ,  $a_1(m)$ , and  $b_1(m)$  are given in the Appendix by Eqs. (A16)–(A18), respectively. Setting the independent term and the coefficients of  $\sin \varphi$  and  $\cos \varphi$  to zero, respectively, one gets the equations for  $A_0$ ,  $A_1$ , and  $B_1$ . The existence of a nontrivial solution requires the determinant of the corresponding coefficient matrix to vanish, i.e.,

$$\begin{vmatrix} \Omega^2 \left( \frac{m}{2} - 1 \right) + 2\varepsilon \frac{a_1(m) - \sqrt{1-m}}{1 - \sqrt{1-m}} & q a_1(m) \\ -q b_1(m) & \Omega^2 \left( \frac{m}{2} - 1 \right) + 2\varepsilon \frac{b_1(m) - \sqrt{1-m}}{1 - \sqrt{1-m}} \end{vmatrix} = 0, \quad (18)$$

which gives [cf. Eq. (6)]

$$F = F^{(1)}(m, T, \eta) \equiv \frac{-\alpha_2(m, T) \pm \sqrt{\alpha_2^2(m, T) - 4\alpha_1(m)\alpha_3(m, T, \eta)}}{\alpha_1(m)}, \quad (19)$$

where

$$\alpha_1(m) \equiv \frac{4[a_1(m) - \sqrt{1-m}][b_1(m) - \sqrt{1-m}]}{(1 - \sqrt{1-m})^2}, \quad (20)$$

$$\alpha_2(m, T) \equiv \frac{8K^2(m)(m/2 - 1)[b_1(m) + a_1(m) - 2\sqrt{1-m}]}{T^2(1 - \sqrt{1-m})}, \quad (21)$$

$$\alpha_3(m, T, \eta) \equiv \frac{16K^4(m)}{T^4} \left( \frac{m}{2} - 1 \right)^2 + \frac{4\eta^2 K^2(m)}{T^2} a_1(m) b_1(m). \quad (22)$$

Now we make the following remarks.

First, for trigonometric pulses ( $m=0$ ), one recovers the first-order approximation (12), as expected.

Second, the first-order approximation (19)–(22) can provide only a preliminary estimate of the stability boundary for the *main* instability tongue such that the narrower the pulse, the worse the accuracy of the theoretical estimate (see Fig. 2). Nonetheless, this approximation reproduces fairly well the stretching of the tongue's tail toward ever higher values of the period as the pulse narrows [see Fig. 2(b)]. Also, the extension of the instability region in the  $T$ - $F$  parameter plane increases as the pulse narrows. This behavior is characterized by an enlargement of the tongues' areas and a simultaneous reduction of their number, as can be seen by comparison of Figs. 2(a) and 2(b). Since the stationary solution ( $x=0, dx/dt=0$ ) is stable over the whole range of the parameters in the limiting case  $m=1$ , one then deduces the exist-

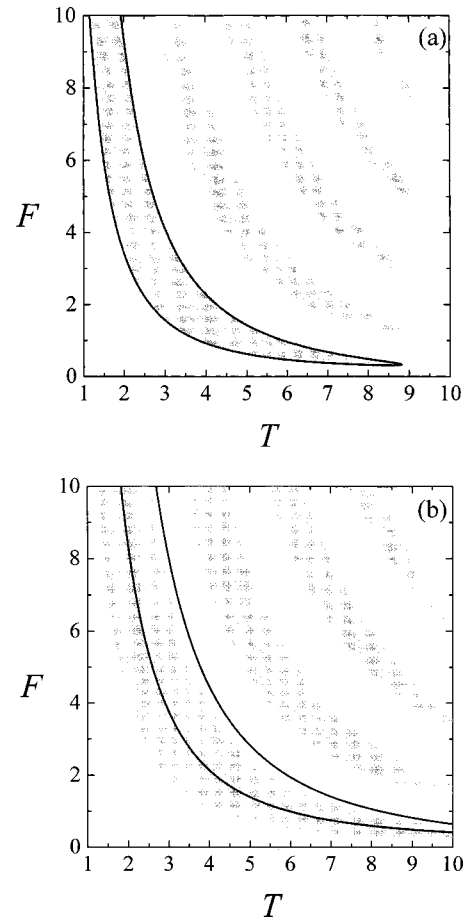


FIG. 2. Stability boundaries of the solution  $x=dx/dt=0$  in the  $T$ - $F$  parameter plane for elliptic pulses [cf. Eq. (4)] and  $\eta=0.2$ . Instability regions (gray areas) were numerically calculated on a grid of  $300 \times 300$  points. Black lines denote the stability boundaries obtained theoretically from Eqs. (19)–(22). (a)  $m=0.5$ . (b)  $m=0.99$ .  $T$  and  $F$  are dimensionless parameters.

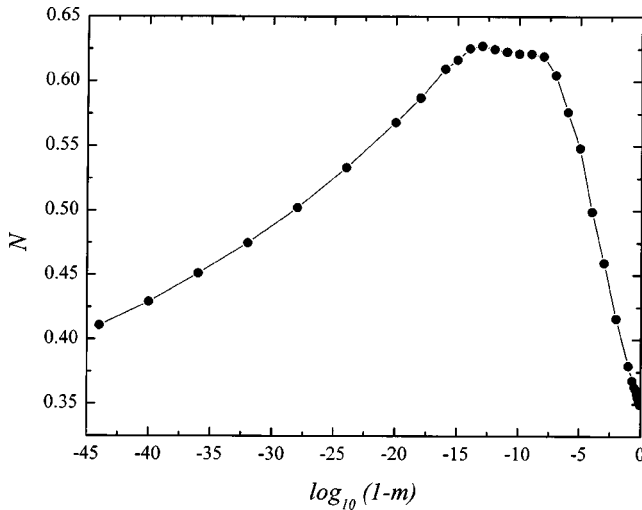


FIG. 3. Fraction of points of the instability regions of the solution  $x=dx/dt=0$  in the  $T$ - $F$  parameter plane,  $N$ , vs the shape parameter  $m$ .  $N$  and  $m$  are dimensionless variables and solid lines are solely plotted to guide the eye.

tence of a (narrow range of) value(s) of the wave form parameter, associated with a certain width of the pulse, for which the extension of the entire instability region is maximal. Figure 3 shows the fraction of points belonging to the instability regions of the stationary solution ( $x=0, dx/dt=0$ ) in the  $T$ - $F$  parameter plane with  $T \in [0.1, 10]$  and  $F \in [0, 10]$  on a  $100 \times 100$  grid,  $N$ , vs the shape parameter  $m$ . One sees indeed that the entire instability region is maximal (after 400 drive cycles) for a shape parameter ranging from  $m \approx 1 - 10^{-8}$  to  $m \approx 1 - 10^{-14}$ . It is worth noting that in this interval the pulse width (measured at half amplitude) is at least 8% of its period. To assess the distribution of transient times to the equilibrium for specified  $\eta$ ,  $F$ , and  $T$ , a grid of  $500 \times 500$  uniformly distributed initial conditions were selected from the phase plane. For each of such initial conditions, we determined the time (measured in drive cycles) required for the NIPKR to evolve to the equilibrium. The accumulated data were then sorted to give the fraction of such initial conditions vs the transient duration. An illustrative example is shown in Fig. 4 for  $\eta=0.2$ ,  $F=2$ ,  $T=6$ , and three values of the shape parameter. We found that, for each value of the shape parameter, the numerically obtained curve accurately fits a sigmoidal Boltzmann function

$$N(n) = A_2 + \frac{A_1 - A_2}{1 + \exp[(n - n_0)/dn]}, \quad (23)$$

where  $A_1 \approx 0$ ,  $A_2 \approx 1$ ,  $d = d(m)$ , and where  $n_0$  provides an estimate of the time at which  $N(n = n_0) = 0.5$  (see Fig. 4). An instantaneous image of the transient basins of the equilibrium after  $t = 25T$  is shown in Fig. 5 for the same parameters as in Fig. 4. Note how the (instantaneous) transient basin becomes ever sparser as the pulse narrows. Figure 6 shows a plot of  $n_0$  (as a parameter characterizing the duration of the transients) vs the shape parameter  $m$  (dots) together with the elliptic fit  $26.02 - \pi/2 + K(m)$ . One sees a clear increase of the duration of the transients as the pulse narrows from its

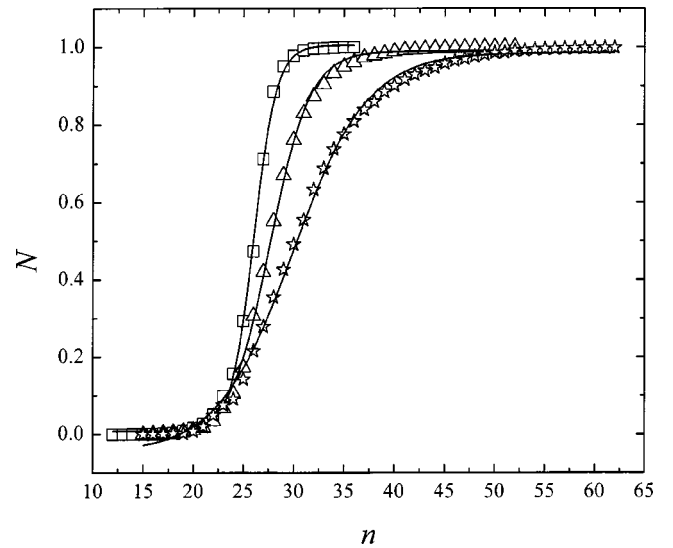


FIG. 4. Fraction of initial conditions  $N$  vs number of drive cycles  $n$  needed to reach the equilibrium  $x=dx/dt=0$  for  $\eta=0.2$ ,  $F=2$ ,  $T=6$ , and three values of the shape parameter:  $m=0$  ( $\square$ ),  $m=0.99$  ( $\triangle$ ), and  $m=0.995$  ( $\star$ ). Also plotted are the corresponding Boltzmann fits [cf. Eq. (23); see the text].  $N$  and  $n$  are dimensionless variables.

trigonometric form. The elliptic fit confirms that the remarkable increase of  $n_0$  from  $m \approx 0.9$  is a consequence of the dependence of the pulse function on the complete elliptic integral of the first kind [cf. Eq. (4)].

Third, the function  $F^{(1)}(m, T = \text{const}, \eta = \text{const})$  presents an overall increasing behavior as the pulse narrows, as expected. Figure 7 shows the instability region in the  $m$ - $F$  parameter plane obtained by numerical calculation and the first-order perturbation stability boundary [Eqs. (19)–(22)]. The first-order approximation qualitatively reproduces the overall form of the stability boundary for the main instability tongue, in particular the expected behavior  $F \rightarrow \infty$  as  $m \rightarrow 1$ . It is clear, however, that the quantitative discrepancies appearing for narrow pulses indicate that higher-order approximations are required for  $m$  close to 1, as well as to obtain the stability boundaries for the secondary tongues.

### C. Comparison with chaotic boundaries

In Ref. [14] it was theoretically and numerically demonstrated that the extension of chaos in parameter space reaches a maximum as the pulse width is varied, which is coherent with the aforementioned results concerning the instability region. Indeed, for fixed wave form and dissipation, the chaotic region in the  $T$ - $F$  parameter plane presents a tongue-like structure which is similar to that of the instability region, as is shown in Fig. 8. Now it is instructive to compare the stability boundaries of the equilibrium with the respective (for each tongue) chaotic boundaries determined by Lyapunov exponent (LE) calculations. We computed LEs by using a version of the algorithm developed in Ref. [31]. In a first step, we calculated the leading LE for each point on a  $100 \times 100$  grid, with period  $T$  and amplitude  $F$  given by the horizontal and vertical axes, respectively. Second, we con-

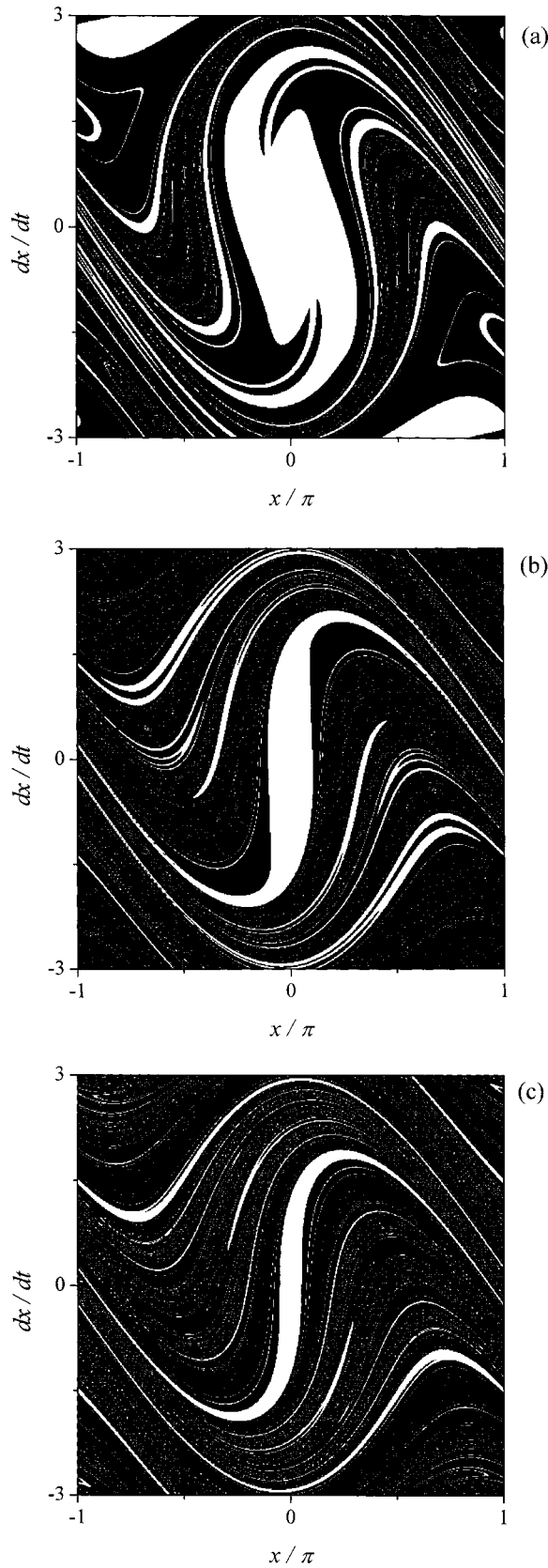


FIG. 5. Transient basins of the equilibrium  $x = dx/dt = 0$  (blank regions) after  $t = 25T$  ( $T$  is the pulse period) for the same parameters as in Fig. 4. (a)  $m = 0$ . (b)  $m = 0.99$ . (c)  $m = 0.995$ .  $x$  and  $dx/dt$  are dimensionless variables.

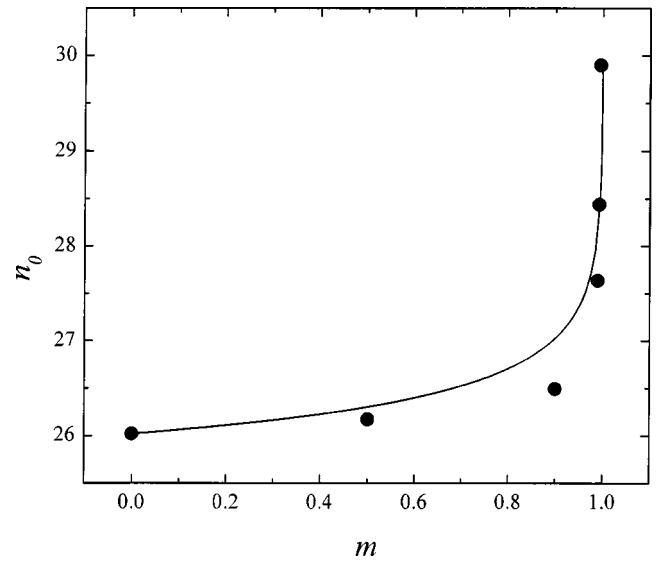


FIG. 6. Plot of  $n_0$  [cf. Eq. (23)] vs the shape parameter  $m$  (dots) along with an elliptic fit (solid line, see the text).  $n_0$  and  $m$  are dimensionless parameters.

structed the diagrams shown in Fig. 4 by plotting a point on the grid only when the corresponding LE was larger than  $10^{-3}$ . One sees that the right-side chaotic boundaries approximately coincide with the right-side stability boundaries, although chaotic tongues are shorter than the corresponding instability tongues. A similar phenomenon was reported in Ref. [32] for a parametrically damped pendulum. The reason for such a coincidence is simple: the common side of both types of boundaries corresponds to a crisis transition in both systems, as will be discussed in the next section. Figure 8 also depicts the theoretical chaotic threshold (solid line)  $U(m, T, F) = 0.2$ , where the chaotic threshold function is

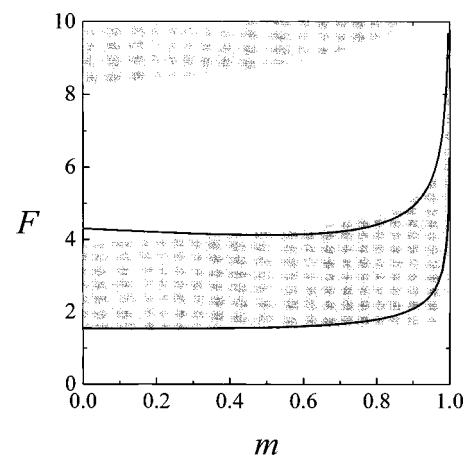


FIG. 7. Stability boundary of the solution  $x = dx/dt = 0$  in the  $m$ - $F$  parameter plane for elliptic pulses [cf. Eq. (4)],  $\eta = 0.2$ , and  $T = 3$ . Instability regions (gray areas) were numerically calculated on a grid of  $300 \times 300$  points. The black lines denote the stability boundaries obtained theoretically from Eqs. (19)–(22).  $m$  and  $F$  are dimensionless parameters.

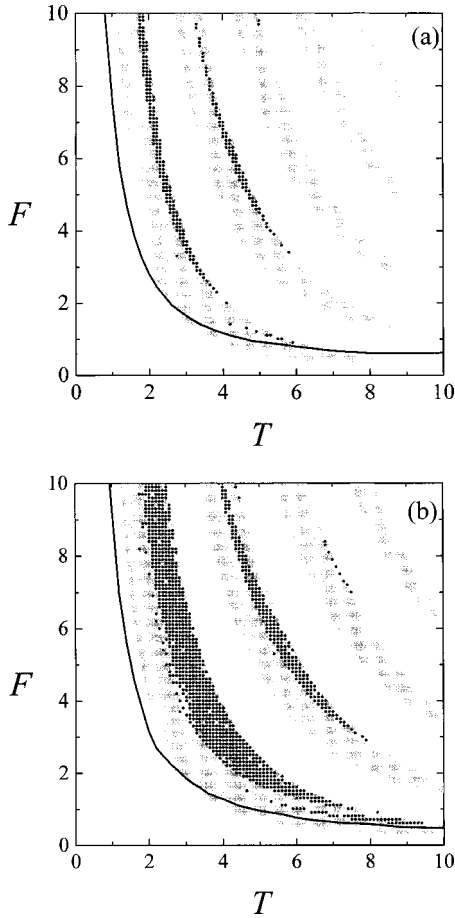


FIG. 8. Instability regions (gray areas) of the solution  $x = dx/dt = 0$  and chaotic regions (black circles) in the  $T$ - $F$  parameter plane for  $\eta=0.2$ . Black lines represent the theoretical chaotic thresholds [cf. Eqs. (24) and (25)] from Melnikov analysis. The instability region (gray areas) was calculated on a grid of  $300 \times 300$  points and the chaotic region on a grid of  $100 \times 100$  points. (a) Trigonometric pulses,  $m=0$ . (b) Elliptic pulses,  $m=0.99$ .

$$U(m, T, F) \equiv \frac{\pi^3}{T^2 \sqrt{F a^3(m)}} \sum_{n=1}^{\infty} n^2 c_n(m) b_n(m, T, F) \quad (24)$$

with

$$a(m) \equiv \frac{\pi/2K(m) - \sqrt{1-m}}{1 - \sqrt{1-m}},$$

$$c_n(m) \equiv \frac{\pi}{(1 - \sqrt{1-m})K(m)} \operatorname{sech} \left[ \frac{n\pi K(1-m)}{K(m)} \right],$$

$$b_n(m, T, F) \equiv \operatorname{csch} \left[ \frac{n\pi^2}{T\sqrt{F a(m)}} \right], \quad (25)$$

which is obtained from Melnikov analysis (MA) (cf. Ref. [14]). As is well known, MA predictions are generally related to transient chaos, which is indeed observed above the predicted threshold  $U(m, T, F) = 0.2$ . Therefore, one cannot ex-

pect too good a quantitative agreement between MA predictions and LE calculations because the LE provides information concerning only steady motions. The chaotic threshold predicted from MA occurs just below the upper left-side stability boundary of the main instability tongue irrespective of the pulse width, as can be seen in Fig. 8. It is worth mentioning that a similar phenomenon is found for a parametrically damped pendulum (cf. Ref. [33]). Although we have not checked the whole parameter space systematically, we have found multiple coexisting attractors inside the instability tongues in the  $T$ - $F$  parameter plane for sufficiently weak dissipation. An illustrative example is depicted in Fig. 9 where one chaotic attractor (black points) and two mutually symmetric period-1 attractors (centers of the circles) are shown together with their respective basins of attraction (gray and blank regions, respectively). For the set of parameters employed ( $T=5.52, F=1, \eta=0.2$ ), we found that the extension of the chaotic attractor diminishes as the shape parameter is increased from  $m=0$  [Fig. 9(a)] to  $m=0.6 \approx m_{\text{threshold}}$  (i.e., very near the chaotic threshold, Fig. 9), while its corresponding basin of attraction does so but to a much lesser extent. For  $m > m_{\text{threshold}}$ , the chaotic attractor disappears, as expected. It is worth mentioning that higher-period attractors have much smaller basins of attraction and, therefore, could not have been detected in our computer simulations.

### III. ORDER-CHAOS ROUTES

In this section we first analyze the bifurcation behavior of the NIPKR [Eqs. (2) and (4)] when solely the pulse width is changed. We chose parameter values for which the rotator is in a chaotic state under trigonometric pulses ( $m=0$ ). An illustrative example is depicted in Fig. 10(a). The global bifurcation diagram was constructed by means of a Poincaré map at the parameters indicated in the caption to Fig. 10. Starting at  $m=0$ , and taking the transient time as 500 excitation periods after every increment of  $\Delta m = 5 \times 10^{-4}$ , we sampled 30 excitation periods by picking up the first  $dx/dt$  value of every excitation cycle. The same initial conditions were set for every  $m$  after  $\Delta m$  was added. The corresponding behavior of the leading LE is displayed in Fig. 10(b). Figure 10(a) shows that over the range  $0 \leq m < 0.268$  the motion of the system is large-scale chaos. Then the system undergoes an inverse interior crisis at  $m \approx m_{\text{ic}} \equiv 0.268$ , limiting the chaotic dynamics to within a smaller region, over the range  $0.268 \leq m < 0.531$ . An inverse attractor merging crisis occurs at  $m \approx m_{\text{iamc}} \equiv 0.531$ , splitting the symmetric chaotic attractor existing over the interval  $0.268 \leq m < 0.531$  into two asymmetric chaotic attractors. These are mutually symmetric because of the NIPKR's symmetry with respect to the transformation ( $x \rightarrow -x$ ), i.e., if  $[x(t), dx(t)/dt]$  is a solution of Eqs. (2) and (4), then so is  $[-x(t), -dx(t)/dt]$ . In other words, nonsymmetric stationary solutions always occur in pairs. For each of the aforementioned inverse (interior and attractor merging) crises, we found crisis-induced intermittency, as expected [34]. Over the range  $0.531 < m \leq 0.599$ , the chaotic dynamics is confined to within an ever smaller region (phase-locked chaos), which is interrupted by periodic

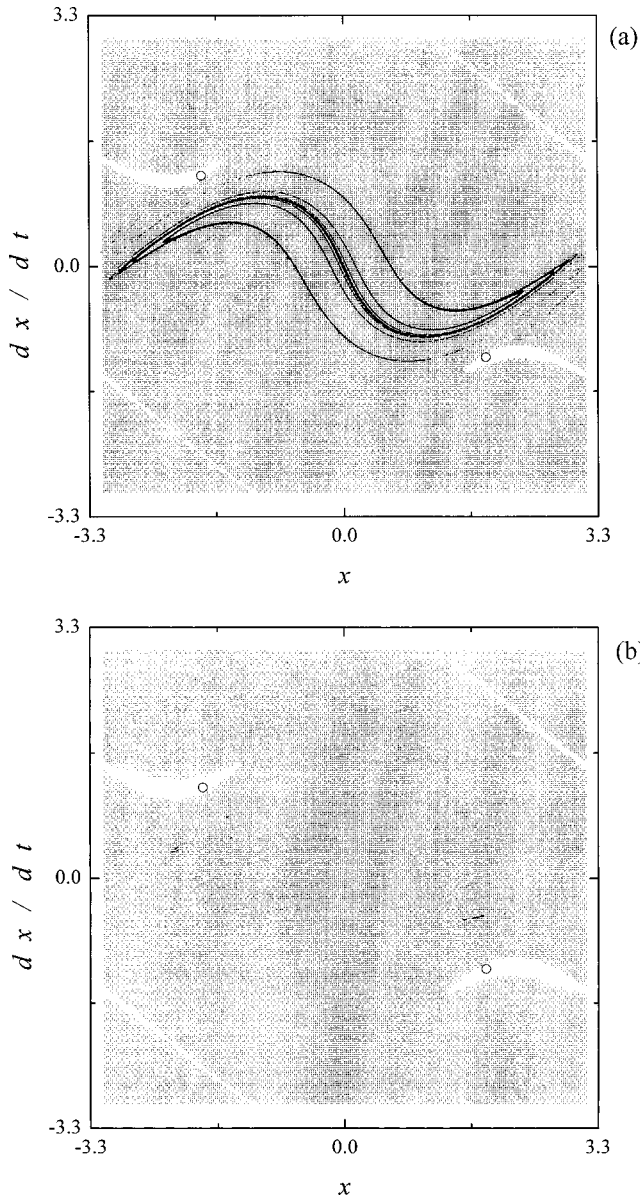


FIG. 9. Multistability for the parameters  $\eta=0.2$ ,  $T=5.52$ , and  $F=1$ . (a)  $m=0$ . (b)  $m=0.6$ , very near the chaos threshold. Chaotic (period-1) attractors are denoted by black points (centers of the circles), while gray (blank) regions represent their basins of attraction. The basins of attraction were calculated on a grid of  $250 \times 250$  points, and  $3 \times 10^4$  points are depicted in each version of the chaotic attractor.  $x$  and  $dx/dt$  are dimensionless variables.

windows. From  $m=0.599$  to  $m=1$  the system's overall behavior is inverse period doubling. The asymmetric period-2 attractor undergoes symmetry restoring at  $m \approx 0.956$ . For  $m \in [0.956, 1]$  there is the steady behavior of a symmetric period-2 attractor, which becomes unstable at a value of  $m$  very close to 1, the equilibrium  $x = dx/dt = 0$  being the resulting attractor. The mechanism underlying the appearance of the aforementioned reshaping-induced crises can be readily understood by studying the simple two-dimensional map

$$z_{n+1} = \alpha z_n + z_n^2 + \beta \text{cn}^2(\Omega \theta_n + \Phi; m),$$

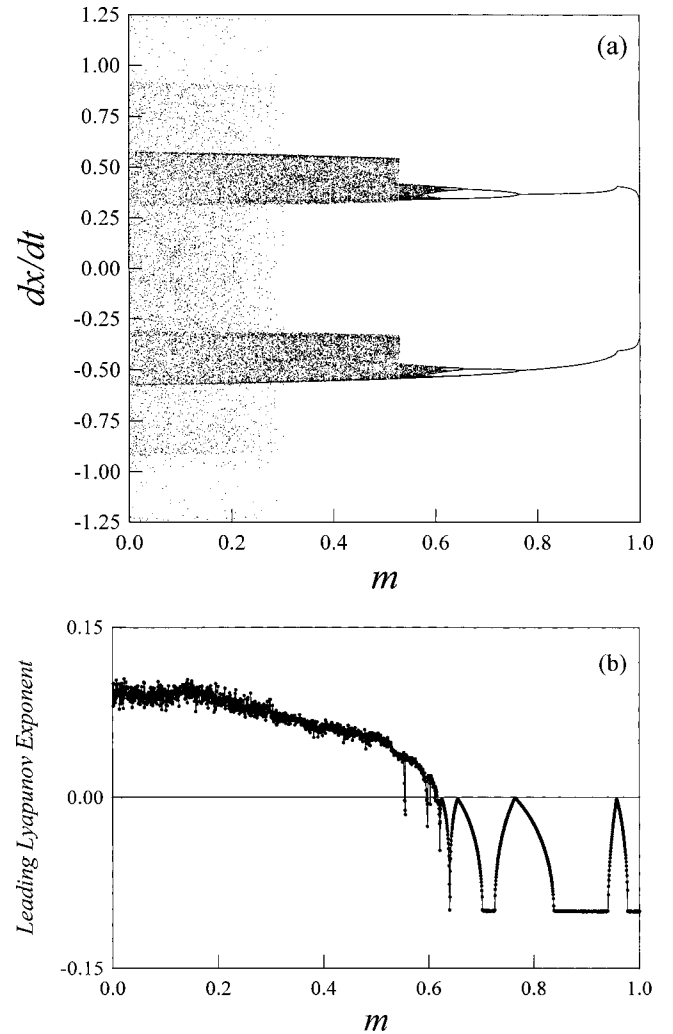


FIG. 10. (a) Bifurcation diagram for the (dimensionless) variable  $dx/dt$  with the (dimensionless) parameter  $m$  in the range  $0 \leq m < 1$ . (b) Values of the leading Lyapunov exponent (dimensionless quantity) as a function of  $m$  in the same range as in (a). NIPKR parameters:  $\eta=0.2$ ,  $F=1$ , and  $T=5.52$ .

$$\theta_{n+1} = 2\theta_n \bmod(2\pi), \quad (26)$$

where  $\alpha$ ,  $\beta$ , and  $\Phi$  are parameters, and  $\text{cn}(\Omega \theta + \Phi; m)$  is the JEF of the parameter  $m$ . Note that the function  $\text{cn}^2(\Omega \theta + \Phi; m)$  represents a pulse function which is similar to that given by Eq. (4). Since we are interested in the case when solely the pulse shape is varied, we fix its period  $T = \text{const}$ , making  $\Omega = \Omega(m) \equiv 2K(m)/T$  and  $\Phi = \Phi(m, \varphi) \equiv 2K(m)\varphi/T$  ( $\varphi \in [0, T]$ ). When  $m=0$ , then  $\text{cn}^2(\Omega \theta + \Phi; m=0) = \cos^2(\pi/T + \pi\varphi/T)$  while, by increasing  $m$ , the effective width of the pulse becomes ever smaller, i.e., the functions  $\text{cn}^2(\Omega \theta + \Phi; m)$  and  $p(t; T, m)$  [cf. Eq. (4)] exhibit the same required properties. Also, for  $m=0$ ,  $\varphi=0$ , and  $T=2\pi$  one recovers a map which is similar to that considered in Ref. [35]. As was the case for that map (cf. Ref. [35]), numerical simulations indicated that, for certain parameter values, the map (26) presents two attractors:  $z = \infty$  (which, for the present purposes, should be regarded as a generic nonchaotic attractor) and a chaotic attractor located in the

region  $z \in [-0.1, 0.1]$ . The nonlinearity in Eq. (26) is the same as in the map studied in Ref. [35], so that the same arguments concerning the appearance of crises carry over to Eq. (26): by looking at the fixed points of Eq. (26), one deduces the critical parameter values  $(\alpha^*, \beta^*, T^*, \varphi^*, m^*)$  for which the two fixed points  $(z, \theta) = \{(z_c, 0), (z_b, 0)\}$  touch (i.e., a crisis occurs), where  $z_b$  is the smallest  $z$  value on the upper ( $z > 0$ ) basin boundary of the attractor  $z = \infty$  while  $z_c$  is the largest  $z$  value on the chaotic attractor. Setting  $\theta = 0$  in Eq. (26) and assuming that  $z_n$  is independent of  $n$ , one has  $z_{\pm} = \{1 - \alpha \pm [(1 - \alpha)^2 - 4\beta \text{cn}^2(2K\varphi/T; m)]^{1/2}\}/2$ , and  $z_b = z_+$ ,  $z_c = z_-$ . Therefore, a crisis occurs when  $z_+ = z_-$ , i.e., for

$$\alpha = \alpha^* \equiv 1 - 2\sqrt{\beta^*} \text{cn} \left[ \frac{2K(m^*)\varphi^*}{T^*}; m^* \right]. \quad (27)$$

Let us suppose that for fixed  $\beta \equiv \beta^*$ ,  $T \equiv T^*$ , and  $\varphi \equiv \varphi^*$  ( $> 0$ ), and  $m \leq 1$  (sharply kicking pulse), one has that the chosen  $\alpha < \alpha^* = \alpha^*(m)$ . As  $m$  is decreased from  $m \leq 1$ ,  $\alpha^*(m)$  decreases so that the two fixed points move toward each other and, in some case that depends upon the choice  $(\beta^*, T^*, \varphi^*, \alpha)$ , coalesce at  $m = m^*$  for which  $\alpha^*(m = m^*) = \alpha$ . Thus, a reshaping-induced crisis occurs as in the NIPKR, the basic underlying mechanism being the same in both cases (but with a pair of periodic orbits for the NIPKR instead of the pair of fixed points).

Second, we shall comment on the bifurcation behavior when solely the period is varied. Figure 11 shows bifurcation diagrams ( $dx/dt$  vs  $T$ ) constructed through a Poincaré map at  $F = 4$ ,  $\eta = 0.2$ , and  $T$  ranging from 0.5 to 10. In this route, the stationary solution  $x = dx/dt = 0$  becomes unstable as the period approaches the boundary of the corresponding instability tongue (compare the homonymous cases in Figs. 8 and 11, respectively). With increasing period, chaos (a strange chaotic attractor) may appear (depending on the specific tongue) by period-doubling bifurcations which are occasionally interrupted (for certain values of the period) by jumps onto coexisting attractors. At even higher periods  $T$ , the strange attractor is destroyed by a boundary crisis at  $T = T_{bc} \equiv T_{bc}(m)$ , the equilibrium  $x = dx/dt = 0$  being the steady state for  $T \gtrsim T_{bc}$ .

#### IV. CONCLUSION

In this paper we have studied the dynamics of a damped kicked rotator subjected to a periodic string of asymmetric single-maximum pulses of finite width and amplitude. It can be expected that the findings remain approximately the same, independently of the particular wave form of the pulses, as long as an invariance condition concerning the impulse transmitted by the pulses is satisfied. The following is a summary of the main results.

(i) The extension of the instability region associated with the equilibrium  $x = dx/dt = 0$  in pulse parameter space reaches a maximum as the pulse width is varied. A preliminary estimate of the stability boundary in the  $m$ - $F$  parameter plane was obtained by means of an elliptic harmonic balance method. These results represent well-behaved dynamical

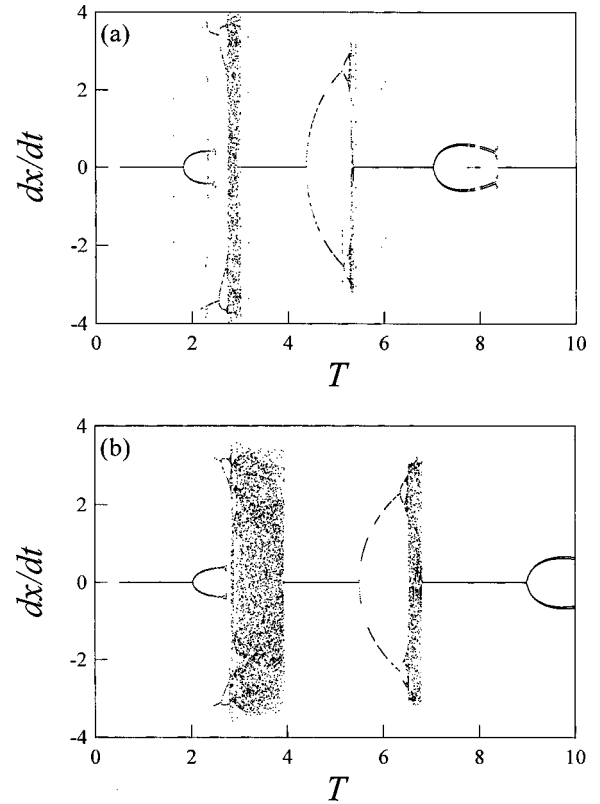


FIG. 11. Bifurcation diagrams for the (dimensionless) variable  $dx/dt$  with the (dimensionless) period  $T$  in the range  $0.5 \leq T \leq 10$ . Parameters are  $F = 4$  and  $\eta = 0.2$ . (a)  $m = 0$ . (b)  $m = 0.99$ .

properties of the NIPKR, in the sense that they are insensitive to the specific wave form of the pulses.

(ii) The stability boundaries of the equilibrium  $x = dx/dt = 0$  in the  $T$ - $F$  parameter plane were estimated, to lowest (arbitrary) perturbative order, for general elliptic (trigonometric) pulses by means of an elliptic (circular) balance method. Numerical calculations indicated that the respective theoretical curves provide (to the tenth-order truncation) excellent approximations for trigonometric pulses, and that they are reliable (to the first-order truncation) for pulse shapes not too far from the trigonometric shape in the case of general elliptic pulses.

(iii) The bifurcation behavior along the stability boundary in the parameter planes  $T$ - $F$  and  $m$ - $F$  were obtained numerically. In particular, the order-chaos route when solely the width of the pulses is altered appears to be especially rich, including different types of crisis.

Finally, we should emphasize that none of the phenomena characterized in this work are present in the classical kicked rotator [4]. The present results could be useful in virtually any scientific field where periodic strings of pulses appear: nonlinear optics and neurosciences are relevant instances. Some interesting open problems remain. Among them, we are presently considering the study of the Hamiltonian version of the NIPKR.

#### ACKNOWLEDGMENTS

We thank Professor J. A. Blackburn for kindly providing a reprint of Ref. [20]. We acknowledge the Ministerio de Cien-

cia y Tecnología of Spain (Project No. BFM2002-00010) for partial financial support.

### APPENDIX: GENERALIZED FOURIER SERIES IN WHICH JACOBIAN ELLIPTIC FUNCTIONS ARE USED

This appendix shows how to obtain the expansions of a periodic function  $f(\tau)$ , with period  $4K(m)$ , in terms of the periodic set of so-called *elliptic harmonics* [29],

$$\begin{aligned}\cos_0(\tau;m) &\equiv 1, & \cos_n(\tau;m) &\equiv \cos(n\varphi), \\ \sin_n(\tau;m) &\equiv \sin(n\varphi),\end{aligned}\quad (\text{A1})$$

where  $\varphi \equiv \text{am}(\tau;m)$ ,  $m < 1$ , and  $n = 1, 2, \dots$ . Therefore, one looks for the Fourier coefficients  $a_n, b_n$  of

$$f(\tau) = \frac{a_0}{2} + \sum_{n=1}^{\infty} [a_n \cos(n\varphi) + b_n \sin(n\varphi)]. \quad (\text{A2})$$

They can be obtained by a standard (trigonometric) Fourier expansion of the transformed function  $f(\varphi;m)$  in terms of  $\cos(n\varphi)$  and  $\sin(n\varphi)$ :

$$a_n(m) = \frac{1}{\pi} \int_0^{2\pi} f(\varphi;m) \cos(n\varphi) d\varphi, \quad (\text{A3})$$

$$b_n(m) = \frac{1}{\pi} \int_0^{2\pi} f(\varphi;m) \sin(n\varphi) d\varphi. \quad (\text{A4})$$

However, instead of changing the function  $f(\tau)$  into the form  $f(\varphi;m)$  [by using the inverse function  $\tau = \text{am}^{-1}(\varphi;m)$ ], the current procedure uses a set of orthogonal functions defined in the  $\tau$  variable [the set (A1)]. One therefore has

$$f(\tau) = \frac{a_0}{2} + \sum_{n=1}^{\infty} [a_n \cos_n(\tau;m) + b_n \sin_n(\tau;m)], \quad (\text{A5})$$

where, upon substituting expression (A1) and the formula  $d\varphi/d\tau = d[\text{am}(\tau;m)]/d\tau = \text{dn}(\tau;m)$  (cf. Ref. [16]) into the expressions (A3) and (A4), one has

$$a_n(m) = \frac{1}{\pi} \int_0^{4K} f(\tau) \cos_n(\tau;m) \text{dn}(\tau;m) d\tau, \quad (\text{A6})$$

$$b_n(m) = \frac{1}{\pi} \int_0^{4K} f(\tau) \sin_n(\tau;m) \text{dn}(\tau;m) d\tau. \quad (\text{A7})$$

Thus, for the function  $\text{dn}(\tau;m)$  and the products of JEFs appearing in Eq. (16), one straightforwardly obtains

$$\text{cn}^3(\tau;m) = \frac{3}{4} \text{cn}(\tau;m) + \dots, \quad (\text{A8})$$

$$\text{sn}(\tau;m) \text{dn}(\tau;m) = b_1(m) \text{sn}(\tau;m) + \dots, \quad (\text{A9})$$

$$\text{cn}(\tau;m) \text{dn}(\tau;m) = a_1(m) \text{cn}(\tau;m) + \dots, \quad (\text{A10})$$

$$\text{sn}^3(\tau;m) = \frac{3}{4} \text{sn}(\tau;m) + \dots, \quad (\text{A11})$$

$$\text{dn}(\tau;m) = a_0(m) + \dots, \quad (\text{A12})$$

where  $E(m)$  is the complete elliptic integral of the second kind [16]. By using Eqs. (A6) and (A7), the coefficients are given by

$$a_0(m) = \frac{1}{\pi} \int_0^{4K} \text{dn}^2(\tau;m) d\tau, \quad (\text{A13})$$

$$a_1(m) = \frac{1}{\pi} \int_0^{4K} \text{cn}^2(\tau;m) \text{dn}^2(\tau;m) d\tau, \quad (\text{A14})$$

$$b_1(m) = \frac{1}{\pi} \int_0^{4K} \text{sn}^2(\tau;m) \text{dn}^2(\tau;m) d\tau. \quad (\text{A15})$$

Finally, with the aid of standard tables [30],  $a_0(m)$ ,  $a_1(m)$ , and  $b_1(m)$  can be written as

$$a_0(m) = \frac{4E(m)}{\pi}, \quad (\text{A16})$$

$$a_1(m) = \frac{4}{3\pi m} [(m+1)E(m) - (1-m)K(m)], \quad (\text{A17})$$

$$b_1(m) = \frac{4}{3\pi m} [(2m-1)E(m) + (1-m)K(m)]. \quad (\text{A18})$$

[1] R. Z. Sagdeev, D. A. Usikov, and G. M. Zaslavskii, *Nonlinear Physics: From the Pendulum to Turbulence and Chaos* (Harwood, New York, 1988).  
 [2] *Chaos in Chemistry and Biochemistry*, edited by R. J. Field and L. Györgi (World Scientific, London, 1993).  
 [3] *Methods in Neuronal Modeling: From Ions to Networks*, edited by C. Koch and I. Segev (MIT Press, Cambridge, MA, 1999).  
 [4] G. M. Zaslavskii, Phys. Lett. **69A**, 145 (1978).  
 [5] M. R. Guevara and L. Glass, J. Math. Biol. **14**, 1 (1982).  
 [6] D. L. González and O. Piro, Phys. Rev. Lett. **50**, 870 (1983).  
 [7] M. Dolnik, I. Schreiber, and M. Marek, Phys. Lett. **100A**, 316 (1984).

[8] M. A. Lieberman and K. Y. Tsang, Phys. Rev. Lett. **55**, 908 (1985).  
 [9] G. A. Cecchi *et al.*, Chaos **3**, 51 (1993).  
 [10] U. Feudel *et al.*, Phys. Rev. E **54**, 71 (1996).  
 [11] A. J. Lichtenberg and M. A. Lieberman, *Regular and Chaotic Dynamics* (Springer, New York, 1992).  
 [12] R. Chacón, J. Math. Phys. **38**, 1477 (1997).  
 [13] A. R. Zeni and J. A. C. Gallas, Physica D **89**, 71 (1995).  
 [14] R. Chacón and A. Martínez García-Hoz, Phys. Lett. A **281**, 231 (2001).  
 [15] R. Chacón, Phys. Rev. E **50**, 750 (1994).  
 [16] See, e.g., L. M. Milne-Thomson, in *Handbook of Mathemati-*

- cal Functions*, edited by M. Abramowitz and I. A. Stegun (Dover, New York, 1972).
- [17] See, e.g., V. I. Arnold, *Mathematical Methods of Classical Mechanics* (Springer, New York, 1987), p. 113.
- [18] J. B. McLaughlin, *J. Stat. Phys.* **24**, 375 (1981).
- [19] B. P. Koch and R. W. Leven, *Physica D* **16**, 1 (1985).
- [20] J. A. Blackburn, H. J. T. Smith, and N. Grønbech-Jensen, *Am. J. Phys.* **60**, 903 (1992).
- [21] D. Capecchi and S. R. Bishop, *Dyn. Stab. Syst.* **9**, 123 (1994).
- [22] M. J. Clifford and S. R. Bishop, *Phys. Lett. A* **201**, 191 (1995).
- [23] J. A. Blackburn, N. Grønbech-Jensen, and H. J. T. Smith, *Phys. Rev. Lett.* **74**, 908 (1995).
- [24] J. Starret and R. Tagg, *Phys. Rev. Lett.* **74**, 1974 (1995).
- [25] R. Chacón, *Phys. Rev. E* **52**, 2330 (1995).
- [26] S.-Y. Kim *et al.*, *Phys. Rev. E* **56**, 6613 (1997).
- [27] See, e.g., E. L. Ince, *Ordinary Differential Equations* (Dover, New York, 1956), pp. 381–384.
- [28] J. Díaz Bejarano and A. Martín Sánchez, *J. Sound Vib.* **134**, 333 (1989); *J. Math. Phys.* **30**, 1871 (1989).
- [29] S. Bravo Yuste, *J. Sound Vib.* **145**, 381 (1991), and references therein.
- [30] P. F. Byrd and M. D. Friedman, *Handbook of Elliptic Integrals for Engineers and Scientists* (Springer-Verlag, Berlin, 1971), p. 303.
- [31] A. Wolf *et al.*, *Physica D* **16**, 285 (1985).
- [32] B. Wu and J. A. Blackburn, *Phys. Rev. E* **45**, 7030 (1992).
- [33] H. J. T. Smith and J. A. Blackburn, *Phys. Rev. A* **40**, 4708 (1989).
- [34] C. Grebogi *et al.*, *Phys. Rev. A* **36**, 5365 (1987).
- [35] C. Grebogi, E. Ott, and J. A. Yorke, *Phys. Rev. Lett.* **50**, 935 (1983).